JOURNAL OF MATERIALS RESEARCH AND TECHNOLOGY 2023;26:8922–8933

Available online at www.sciencedirect.com

jmr&t
Journal of Materials Research and Technology

journal homepage: www.elsevier.com/locate/jmrt

Phase field simulation of eutectoid microstructure during austenite-pearlite phase transformation

Shaojie Lv [a], Hong-Hui Wu [a,b,c,*], Kaiyang Wang [a], Chaolei Zhang [a,b,**], Jiaming Zhu [c,d], Shuize Wang [a,b,***], Guilin Wu [a,b], Junheng Gao [a,b], Xu-Sheng Yang [e], Xinping Mao [a,b]

[a] *Beijing Advanced Innovation Center for Materials Genome Engineering, Research Institute for Carbon Neutrality, University of Science and Technology Beijing, Beijing 100083, China*
[b] *Institute of Steel Sustainable Technology, Liaoning Academy of Materials, Shenyang 110004, China*
[c] *Institute of Materials Intelligent Technology, Liaoning Academy of Materials, Shenyang 110004, China*
[d] *School of Civil Engineering, Shandong University, Jinan 250061, China*
[e] *Department of Industrial and Systems Engineering, The Hong Kong Polytechnic University, Hong Kong, China*

ARTICLE INFO

Article history:
Received 16 June 2023
Accepted 20 September 2023
Available online 24 September 2023

Keywords:
Phase-field simulation
Austenite-pearlite transformation
Cooling rate
Isothermal temperature
Mn content

ABSTRACT

Pearlitic steel, known for its superior strength, plasticity and wear resistance, is widely used in diverse applications including light rail, spring production, wire manufacturing, high-rise constructions, etc. The pearlite phase transformation involves a complex transformation process of three phases and two interfaces, and its phase transformation process and complex physical nature necessitate further exploration and study. In this work, the austenitic-pearlite transformation in Fe-0.77C wt.% binary alloys and Fe-0.7C-xMn ($x = 0.1, 0.2, 0.3$) wt.% ternary alloys were examined by using a CALPHAD-based multicomponent multi-phase-field model. The effects of isothermal transformation temperature, cooling rate, and Mn content on the microstructure evolution during the austenite-pearlite transformation were discussed. Furthermore, the multi-component diffusion is captured by phase-field modeling of the lamellar pearlite growth. The current findings offer a novel perspective for investigating the pearlite microstructure in relation to varied compositions and heat treatment processes.

1. Introduction

Pearlite is a product of the eutectoid transformation of austenite, typically presenting alternating lamellar arrangements of cementite and ferrite [1–4]. This transformation process is characterized by the cooperative growth of ferrite and cementite, each sharing a phase boundary with austenite. Given the compositional inhomogeneity and energy fluctuation in supercooled austenite, the regions deficient in carbon and those rich in carbon may serve as nucleation locations for

---

* Corresponding author. Beijing Advanced Innovation Center for Materials Genome Engineering, Research Institute for Carbon Neutrality, University of Science and Technology Beijing, Beijing 100083, China.
** Corresponding author. Beijing Advanced Innovation Center for Materials Genome Engineering, Research Institute for Carbon Neutrality, University of Science and Technology Beijing, Beijing 100083, China.
*** Corresponding author. Institute of Steel Sustainable Technology, Liaoning Academy of Materials, Shenyang 110004, China.
E-mail addresses: wuhonghui@ustb.edu.cn (H.-H. Wu), zhangchaolei@ustb.edu.cn (C. Zhang), wangshuize@ustb.edu.cn (S. Wang).

https://doi.org/10.1016/j.jmrt.2023.09.201

Table 1 – The values of relevant parameters used in the multi-phase-field model.

Symbol	Parameter	Value	Unit
$dx = dz$	Simulation size	50	μm
Nx = Nz	Grid number	500	/
Δx	Grid resolution	0.1	μm
η	Interface thickness	$5\Delta x$	μm
$V_m(\gamma)$	Molar volume	7.18×10^{-6}	$m^3 \cdot mol^{-1}$
$V_m(\alpha)$		7.27×10^{-6}	
$V_m(\theta)$		7.0×10^{-6}	
$\sigma_{\gamma,\ \gamma}$	Interface energy	7.6×10^{-1}	$J \cdot m^{-2}$
$\sigma_{\gamma,\ \alpha}$		7.2×10^{-1}	
$\sigma_{\gamma,\ \theta}$		6.7×10^{-1}	
$\sigma_{\alpha,\ \alpha}$		7.6×10^{-1}	
$\sigma_{\alpha,\ \theta}$		7.1×10^{-1}	
$\sigma_{\theta,\ \theta}$		7.6×10^{-1}	
$\mu_{\gamma,\ \gamma}$	Kinetic coefficient	1.0×10^{-13}	$m^4 \cdot J^{-1}$
$\mu_{\gamma,\ \alpha}$		1.0×10^{-14}	
$\mu_{\gamma,\ \theta}$		1.0×10^{-11}	
$\mu_{\alpha,\ \alpha}$		1.0×10^{-16}	
$\mu_{\alpha,\ \theta}$		1.0×10^{-16}	
$\mu_{\theta,\ \theta}$		1.0×10^{-13}	

cementite and ferrite, respectively. Predominantly, the formation of pearlitic crystal nuclei occurs at the boundaries of austenite grains [5–7]. In light of the broad applicability of pearlitic steels, pearlite phase transformation has been a key subject of extensive research for several decades, encompassing both experimental and theoretical investigations into eutectoid decomposition in steels [8–14].

Numerous studies have been conducted to experimentally investigate the pearlitic phase transformation. For instance, to scrutinize the concentration distribution at the austenite/pearlite interface, Aranda et al. [15] analyzed the C and Mn diffusion mechanism during the pearlite phase transformation process. The results demonstrated that the Mn content within the cementite and ferrite phases increases as the austenite-to-pearlite growth process progressed. In a separate study, Miyamoto et al. [16] explored the influences of C content and phase transformation temperature on the microstructure of high C steel during isothermal phase transformation, specifically focusing on the Fe-1Mn-(0.75,1.05) C wt.% ternary alloy. Despite these extensive studies, accurately measuring the nucleation rate through experiments poses substantial difficulties, rendering the study of pearlite nucleation and growth a subject of continued debate.

The phase-field model, based on the Ginzburg-Landau free energy functional theory, is primarily utilized to investigate the temporal and spatial evolution of microstructures, and predict the emergence of complex morphologies [17–25]. This method has proven to be a powerful research tool in capturing the solid-state phase transformation process [26–31] and has been used in pearlite phase transformation [9,32–35]. To study the cooperative growth of eutectoid steel pearlite, Nakajima et al. [32] simulated lamellar spacing and growth rates under various

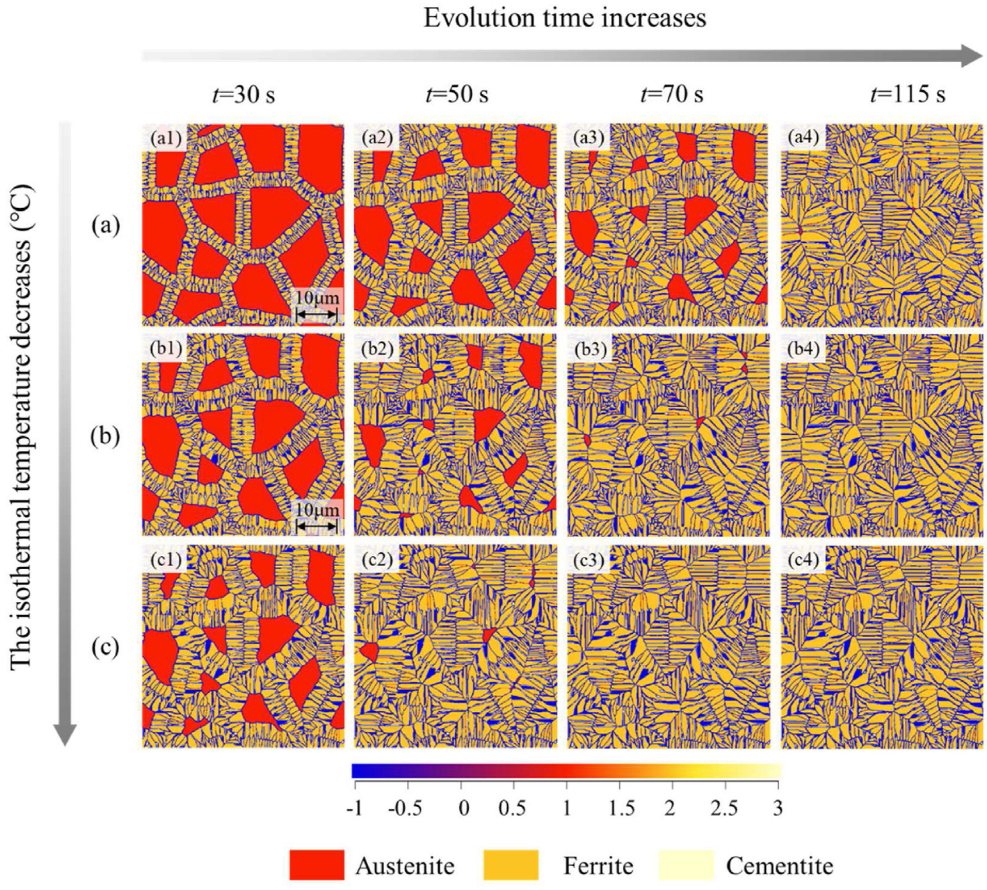

Fig. 1 – Microstructure evolution during the austenite-pearlite transformation under the influence of varied isothermal temperatures: (a) 710 °C, (b) 700 °C, and (c) 690 °C.

supercooling conditions by considering the C diffusion in austenite and ferrite. The simulation found that C diffusion in ferrite and the growth of cementite from the ferrite enhance the growth kinetics of the pearlitic transformation by a factor of four as compared to the growth rate of cementite from austenite. To study the C diffusion along grain boundaries of the pearlite growth rate, Yamanaka [36] et al. employed a phase-field method and calculated the pearlite transformation accompanied by C diffusion in Fe-C-Mn ternary alloys. The results suggested that C diffusion at grain boundaries can enhance the cooperative growth between the ferrite phase and cementite phase, thereby determining the growth rate of the pearlite phase. However, phase-field simulations of the austenite-pearlite transformation have so far been limited to single crystals, and no systematic investigations having been carried out on the austenite-pearlite transformation process in polycrystals of pearlitic steel.

The cellular automata method enables the integration of local concentration changes into nucleation or growth functions, and the use of hexagonal grids can better simulate isotropic phenomena, resulting in a more natural and realistic model. However, the cellular automata model has certain limitations, such as the neglect of interfacial energy effects on phase transformation and the complexity associated with representing and displaying hexagonal grids. The Monte Carlo approach offers the advantage of being less constrained by geometric conditions, possessing convergence speed independent of problem dimensionality, and having a relatively simple program structure for ease of implementation. Conversely, this method can suffer from slow convergence speed and potential probabilistic errors, which may limit its application in certain scenarios. The phase field model couples the phase field with temperature, solute fields, and other external influences effectively bridging the micro and macro scales. A particular strength of the phase field model is its ability to easily handle solute aggregation and second-phase precipitation on grain boundaries, as it does not require the tracing of grain boundary locations.

In the current study, the austenite-pearlite transformation process of Fe-0.77C wt.% binary alloy and Fe-0.7C-xMn ($x = 0.1$, 0.2, 0.3) wt.% ternary alloys in a polycrystalline context of pearlitic steel was simulated by a multi-phase-field model [37–39]. The effects of isothermal temperature, phase transformation cooling rate, and Mn concentration on the microstructure evolution and phase transformation kinetics were analyzed. Furthermore, the physical phenomenon of component diffusion was captured through phase-field simulations of lamellar pearlite growth. The objective of this study is to further elucidate the mechanism of the austenite-to-pearlite transformation and the influence of alloy diffusion on the phase transformation kinetics. By extending the current study, a variety of pearlitic microstructures with different compositions and heat treatments can be predicted.

2. Simulation methodology

2.1. *Model formulations*

The current work employs a multi-phase-field (MPF) model, integrated with thermodynamic databases (TCFE 10) and extended to include linear elasticity. The expression form of the MPF model [39–47] can be divided into chemical free energy density contribution (f_{chem}) and the grain boundary energy density (f_{int}),

$$F = \int_V (f_{chem} + f_{int})\, dV \tag{1}$$

The chemical free energy density contribution is defined as follows,

$$f_{chem} = \sum_{\alpha=1}^{n} \varphi_\alpha f_\alpha(c_\alpha) + \mu\left(c - \sum_{\alpha=1}^{n} \varphi_\alpha c_\alpha\right) \tag{2}$$

where $f_\alpha(c_\alpha)$ indicates the bulk free energies of phase α, which is dependent on the phase concentrations c_α, n indicates the number of phases in the simulated system, and μ represents the generalized chemical potential.

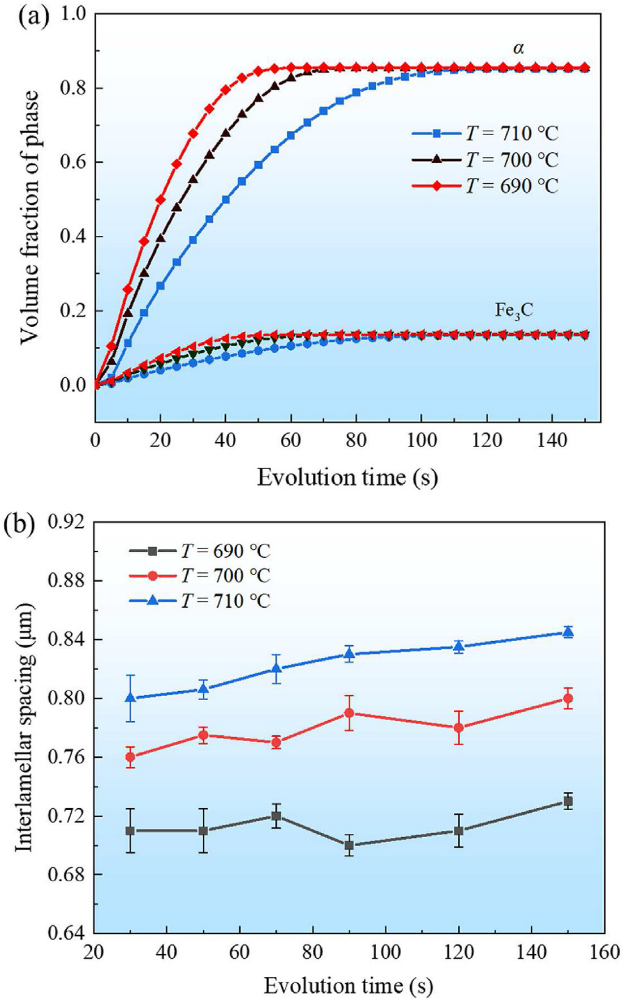

Fig. 2 – Characteristics of microstructure evolution during the austenite-pearlite transformation, (a) evolution curves of ferrite and cementite phase volume fractions with respect to isothermal temperature during austenite-pearlite phase transformation, (b) interlamellar spacing of pearlite as a function of both isothermal temperature and evolution time.

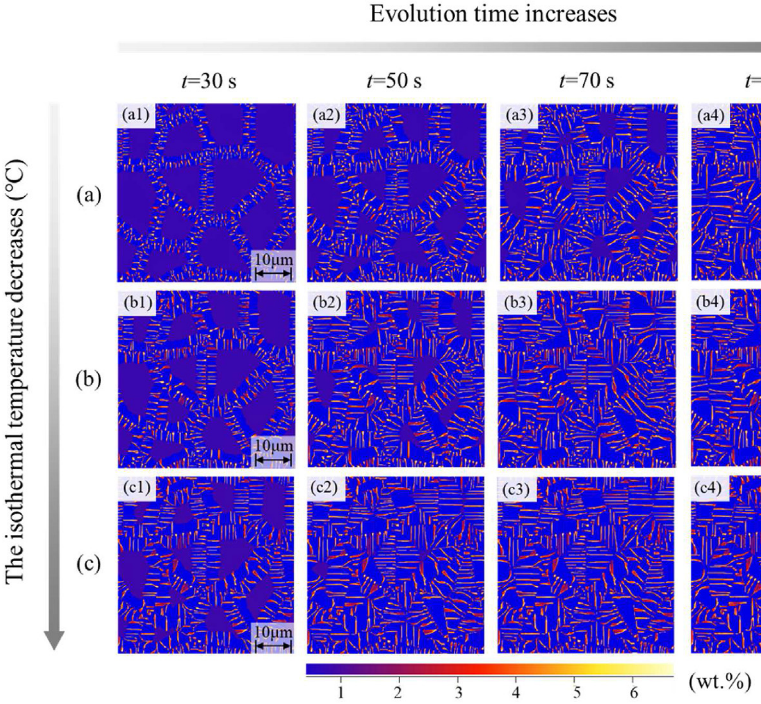

Fig. 3 – Temporal evolution of carbon concentration at various isothermal temperatures, (a) 710 °C, (b) 700 °C, (c) 690 °C.

The contribution of the grain boundary energy density is,

$$f_{\mathrm{int}} = \sum_{\alpha,\beta=1,\alpha\neq\beta}^{n} \frac{4\sigma_{\alpha\beta}}{\eta_{\alpha\beta}} \left(\frac{\eta_{\alpha\beta}^{2}}{\pi^{2}} \left| \nabla\varphi_{\alpha} \nabla\varphi_{\beta} \right| + W_{\alpha\beta} \right) \tag{3}$$

where $\sigma_{\alpha\beta}$ denotes the phase interface energy, or the grain boundary energy between grains with different orientations. $\eta_{\alpha\beta}$ represents the interface thickness of α and β phase, $W_{\alpha\beta}$-$= \varphi_{\alpha}\varphi_{\beta}$ is the phase transformation potential function, and the phase interface energy divided by the interface width is defined as the volumetric energy density [48–50],

The kinetic equations governing the phase field variable based on free energy functional can be expressed as,

$$\frac{\partial\varphi_{\alpha}}{\partial t} = \sum_{\alpha\neq\beta}^{n} \mu_{\alpha\beta}(\vec{n}) \left[\sigma_{\alpha\beta}^{*}(\vec{n}) K_{\alpha\beta} + \frac{\pi}{\eta_{\alpha\beta}} \sqrt{\varphi_{\alpha}\varphi_{\beta}}\, \Delta G_{\alpha\beta}^{chem} \right] \tag{4}$$

$$K_{\alpha\beta} = \left(\varphi_{\alpha} \nabla^{2} \varphi_{\beta} - \varphi_{\beta} \nabla^{2} \varphi_{\alpha} \right) + \frac{\pi^{2}}{\eta_{\alpha\beta}^{2}} \left(\varphi_{\alpha} - \varphi_{\beta} \right) \tag{5}$$

$$\Delta G_{\alpha\beta}^{chem} = -\left(\frac{\partial f^{chem}}{\partial\varphi_{\alpha}} - \frac{\partial f^{chem}}{\partial\varphi_{\beta}} \right) = -f_{\alpha}(c_{\alpha}) + f_{\beta}(c_{\beta}) + \mu(c_{\alpha} - c_{\beta}) \tag{6}$$

where $\mu_{\alpha\beta}$ represents the interfacial mobility between adjacent phases, $\vec{n}$ is the interface orientation, $\sigma_{\alpha\beta}^{*}$ represents the interfacial energy, $K_{\alpha\beta}$ denotes the generalized curvature operator of the interface, $\Delta G_{\alpha\beta}^{chem}$ denotes the chemical driving force, and f_{α} denotes the chemical free energy density within the α phase.

The diffusion equations of the concentration c is,

$$\frac{\partial c}{\partial t} = \nabla \cdot \left(\sum_{\alpha=1}^{n} \varphi_{\alpha} D_{\alpha} \nabla c_{\alpha} \right) \tag{7}$$

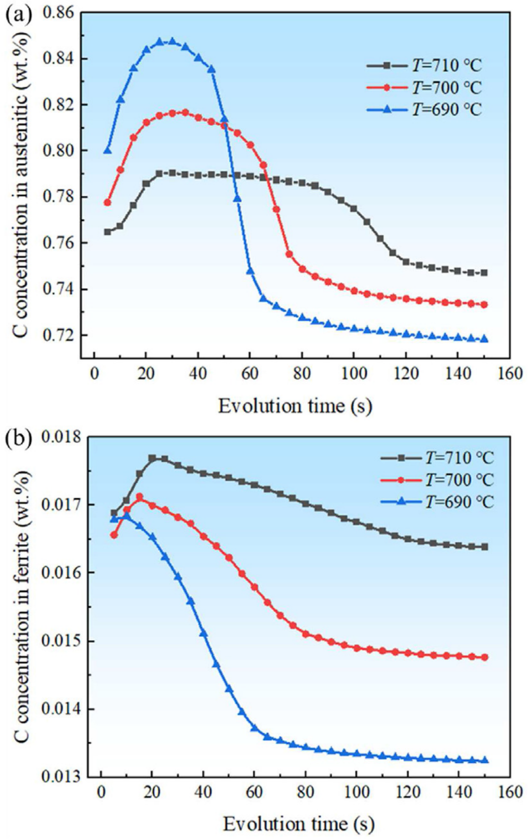

Fig. 4 – Distribution of average C concentration in each phase at various isothermal temperatures, (a) distribution of C concentration in the austenite phase, (b) distribution of C concentration in the ferrite phase.

$$c = \sum_{\alpha=1}^{n} \varphi_\alpha c_\alpha \tag{8}$$

where D_α denotes the diffusion coefficient of the phase α, while the c represents a concentration mixture of different phases. c_α denotes the concentration of a specific phase α.

Equations (4) and (8) are solved utilizing an explicit finite-difference method. These equations are solved using the commercial software MICRESS® (the microstructure evolution simulation software).

2.2. *Simulation methodology*

The current work studies the eutectoid transformation of polycrystalline Fe-0.77C wt.% binary alloys and Fe-0.7C-xMn ($x = 0.1, 0.2, 0.3$) wt.% ternary alloys via MPF simulation. In the MPF model, the concentration field is coupled with the phase field, meanwhile, periodic boundary conditions are applied. The simulation dimension is set at $dx = dz = 50$ μm, with a grid resolution of 0.1 μm, and an interface thickness of $5\Delta x$. The initialization of the microstructure is random, and the austenite, ferrite, and cementite within the simulation domain are isotropic. Considering the interaction force between each phase, the nucleation positions of ferrite and cementite are set to interface nucleation, with austenite as the reference phase. In our current study, Thermo-Calc has been employed to facilitate the coupling with the thermodynamic database, thereby enabling us to use the phase diagram over a wide temperature range. We do not explicitly prescribe the number of phases nucleation. Instead, we leverage a 'shielding effect' to modulate nucleation propensity [23,51,52]. This approach involves a shielding time of 1.0 s and a shielding distance of 1.0 μm. We have also designated a time interval of 0.25 s. The minimum supercooling is set to 5 °C, employing an automatic-limited time step and utilizing the fd-correction method for numerical calculation [53,54]. To ensure the statistical reliability of the pearlite interlamellar spacing during the austenite-pearlite phase transformation process, a fixed austenite phase boundary was strategically selected for statistical analysis within this research. The analysis consisted of six different data sets, with respect to distinct isothermal temperatures and cooling rates. For each data point within these sets, we conducted at least three individual counts to enhance the accuracy of our findings, and error bars were incorporated to transparently convey the potential variability in the data collection process. The values of relevant parameters in the MPF model are presented in Table 1.

3. Numerical results and discussion

3.1. *Influence of isothermal temperature on austenite-pearlite transformation*

To examine the effect of isothermal temperature on the austenite-pearlite transformation, the microstructure evolution of Fe-0.77C wt.% binary alloy during the austenite-pearlite transformation at 710 °C, 700 °C, and 690 °C is

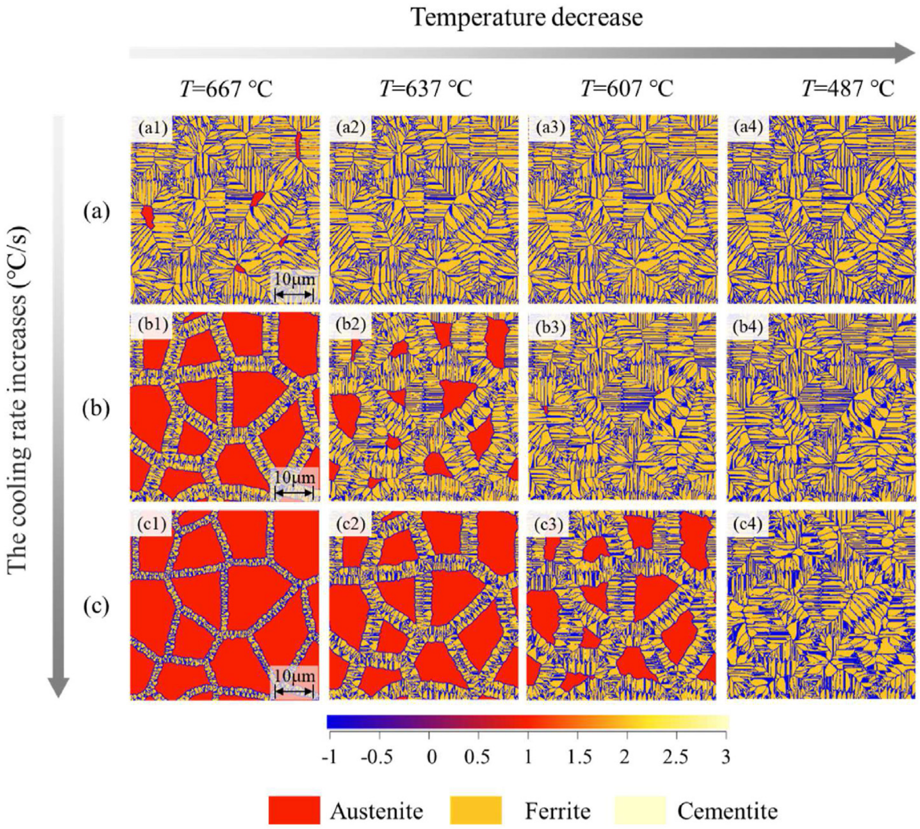

Fig. 5 – The effect of cooling rate *v* of (a) 1 °C/s, (b) 3 °C/s, (c) 6 °C/s on the microstructure of the austenite-pearlite transformation.

illustrated in Fig. 1. When the isothermal temperature during austenite-pearlite transformation is kept a constant, pearlite grows in a lamellar manner over time, with minor divergence occurring during the growth process. When the evolution time is constant, it is observed that the driving force for pearlite transformation amplifies with decreased isothermal temperature. Consequently, the transformation dynamics, and the phase volume fraction of the pearlite both increase. These simulation results underscore the significant influence of isothermal temperature on the microstructural evolution during the pearlite transformation.

As illustrated in Fig. 2(a), the evolution curves for the phase volume fraction of ferrite and cementite are plotted against both isothermal temperature and phase transformation time during the austenite-pearlite transformation process. All three sets of isothermal temperatures selected in the simulation are all below the eutectoid temperature. Therefore, ferrite and cementite will start to nucleate at the onset of the isothermal stage. As the isothermal temperature decreases, the driving force of the austenite-pearlite transformation increases, accelerating the transformation rate. At an isothermal temperature of T = 690 °C, the phase volume fraction of cementite and ferrite achieves its maximum, completing the phase transformation within t = 60 s. Conversely, as the isothermal temperature increases to T = 710 °C, the evolution time required for the phase transformation's completion extends to t = 115 s.

Fig. 2(b) shows the evolution curve of pearlite interlamellar spacing with respect to different isothermal temperatures and evolution time. The results reveal that the distribution range of pearlite interlamellar spacing is 0.70–0.73 μm at the temperature T = 690 °C, representing the smallest spacing at the selected isothermal temperatures. As the isothermal temperature rises to T = 700 °C and T = 710 °C, the distribution range expands to 0.76–0.80 μm and 0.745–0.805 μm, respectively, wherein the pearlite interlamellar spacing fluctuates with the increase of phase transformation evolution time. The current work suggests that the evolution time of the phase transformation will cause a slight increase in the interlamellar spacing of pearlite. This study shows that under identical austenitizing conditions, the interlamellar spacing of pearlite reduces as the austenite-pearlite isothermal temperature decreases.

Fig. 3 illustrates the distribution of C concentration in austenite, ferrite, and cementite under isothermal temperatures of 710 °C, 705 °C, and 700 °C, wherein the bright, dark blue, and purple parts represent the distribution of C concentration in cementite, ferrite, and austenite, respectively. The simulation results indicate that, at a specific phase transformation temperature, the C concentration in cementite increase as the austenite-to-pearlite transformation progresses. Moreover, at a given phase transformation time, a reduced isothermal temperature accelerates the austenite-pearlite phase transformation, resulting in a richer distribution of C concentrations.

To elucidate the diffusion of C concentration in austenite-pearlite transformation, Fig. 4 presents the evolution curves of the average distribution of C concentration in the austenite and ferrite phases as a function of transformation time and various isothermal temperatures. Our findings indicate that the average C concentration in austenite initially increases and then subsequently decreases, with this change being more pronounced at lower isothermal temperatures. As depicted in Fig. 4(a), with the decrease of isothermal temperature from 710 °C to 690 °C, the peak value of C concentration in austenite reaches 0.79 wt.%, 0.815 wt.%, and 0.845 wt.%, respectively. During the initial stage of the austenite-pearlite transformation (0–20 s), the C concentration within the austenite phase surges, and then starts to decline with the phase transformation time further increases. At lower isothermal temperatures, the austenite-pearlite transformation rate accelerates, thereby leading to a rapid decrease of the C concentration in austenite. As illustrated in Fig. 4(b), with the decrease of isothermal temperature, the peak value of C concentration in ferrite reaches 0.0177 wt.%, 0.0171 wt.%, and 0.0168 wt.%, respectively. At lower isothermal temperatures, the driving force for the austenite-pearlite transformation increases, which accelerates the transformation rate and leads to the rapid diffusion of C concentration from the ferrite phase into the austenite phase. Consequently, during the austenite-pearlite transformation process at low isothermal temperatures, the average C concentration in austenite exhibits a larger evolutionary trend, whereas the

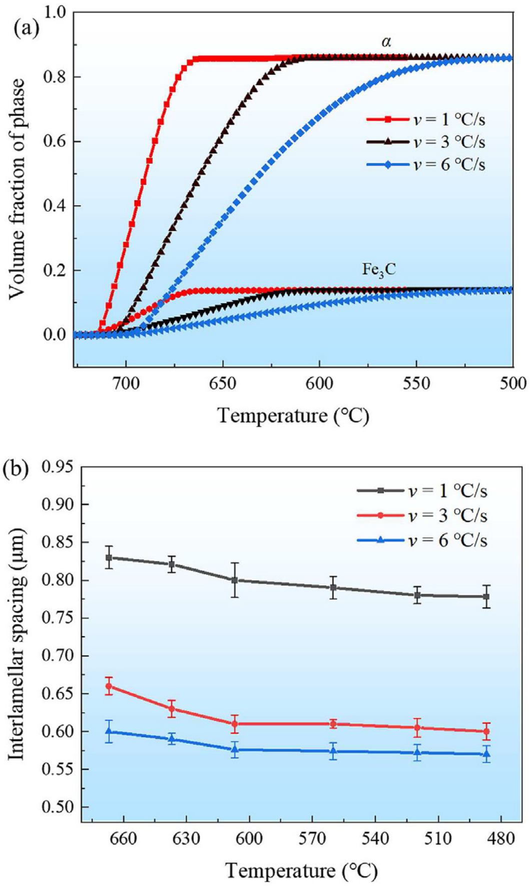

Fig. 6 – Characteristics of the austenite-pearlite transformation, (a) evolution curves of ferrite and cementite volume fractions as a function of cooling rate during austenite-pearlite transformation, (b) evolution curves of pearlite interlamellar spacing as a function of cooling rate and phase transformation evolution time.

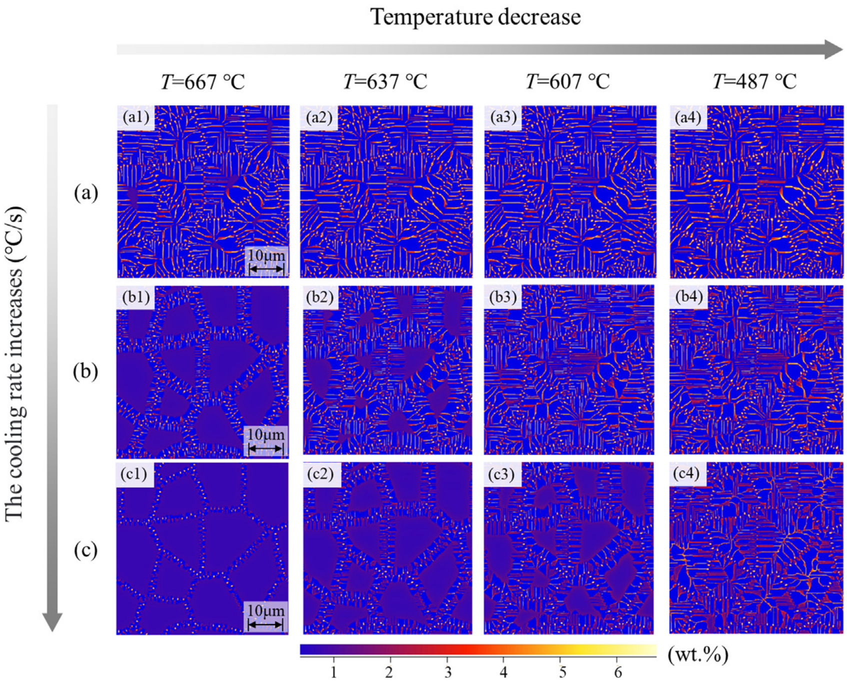

Fig. 7 – The influence of cooling rate υ of (a) 1 °C/s, (b) 3 °C/s, (c) 6 °C/s on the evolution of C concentration.

evolutionary trend of C concentration in ferrite is less pronounced.

3.2. *Influence of cooling rate on austenite-pearlite transformation*

To study the effect of cooling rate on the austenite-pearlite transformation, Fig. 5 demonstrates the microstructural evolution of pearlite at three different cooling rates, namely $\upsilon = 1$ °C/s, $\upsilon = 3$ °C/s, and $\upsilon = 6$ °C/s. The results reveal that at constant cooling rates during pearlite transformation, the nucleation and growth of pearlite, i.e., the ferrite and cementite phases, proceed from the austenite interface. At the phase transformation temperature of $T = 487$ °C, a complete pearlite microstructure composed of interlamellar ferrite and cementite is formed, as illustrated in Fig. 5 (c4). As depicted in Fig. 5 (a), at a constant phase transformation temperature, a slower cooling rate during the austenite-pearlite transformation ($\upsilon = 1$ °C/s) yields a smaller temperature gradient, promoting easier nucleation of the pearlite transformation. Conversely, as shown in Fig. 5(c), an increase in the cooling rate from 1 °C/s to 6 °C/s necessitates a higher degree of undercooling for pearlite nucleation, consequently prolonging the time required to complete the austenite-pearlite transformation.

Fig. 6 presents the austenite-pearlite transformation kinetics and pearlite interlamellar spacing. Fig. 6(a) depicts the kinetic curve of pearlite phase volume fraction (comprising ferrite and cementite) as a function of the cooling rate and phase transformation temperature. The calculation results indicate that at cooling rates of $\upsilon = 1$ °C/s, $\upsilon = 3$ °C/s, and $\upsilon = 6$ °C/s, the corresponding phase transformation temperatures after the pearlite phase transformation are 662 °C, 600 °C, and 500 °C, respectively. Upon completion of the

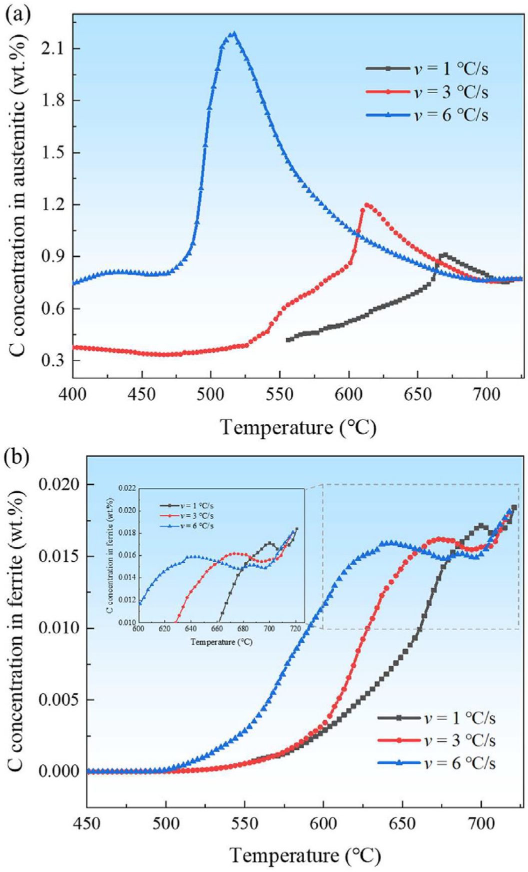

Fig. 8 – The distribution of average C concentration within each phase at different cooling rates, (a) C concentration distribution within the austenite phase, (b) C concentration distribution within the ferrite phase.

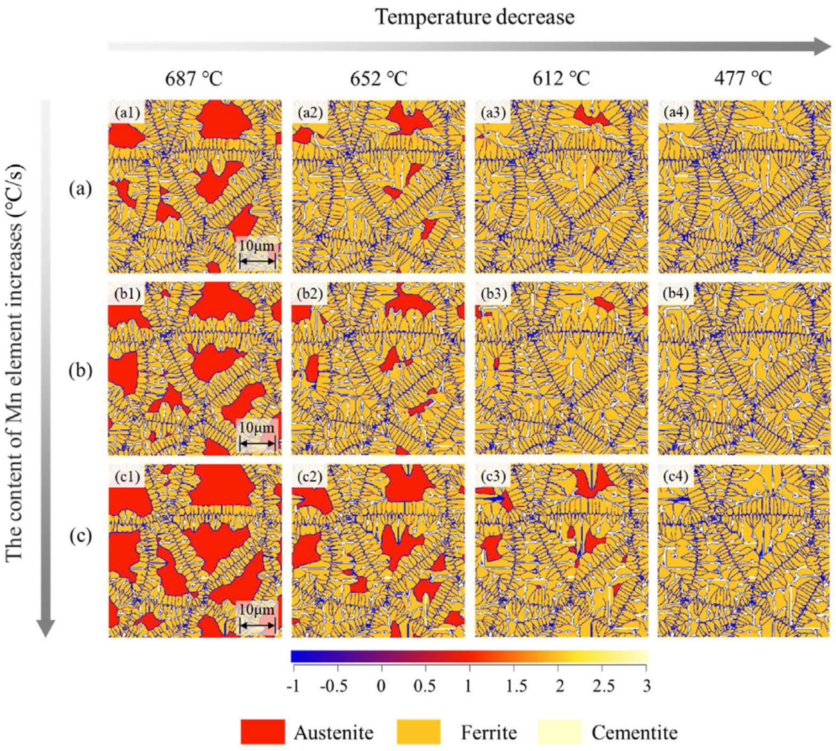

Fig. 9 – The influence of Mn content, (a) Fe-0.7C-0.1Mn wt.%, (b) Fe-0.7C-0.2Mn wt.%, (c) Fe-0.7C-0.3Mn wt.%, on the evolution during the austenite-to-pearlite transformation under a cooling rate of $\upsilon = 1$ °C/s.

pearlite transformation, the ferrite and cementite phase volume fractions are 0.855 and 0.145, respectively, rendering a phase volume ratio of ferrite to cementite 5.6. Fig. 6 (b) outlines the variation in pearlite interlamellar spacing as a function of the cooling rate and phase transformation temperature. The results suggest that the pearlite interlamellar spacing decreases as the cooling rate of pearlite transformation increase.

Fig. 7 illustrates the evolution of the C concentration as a function of transformation temperature at cooling rates of $\upsilon = 1$ °C/s, $\upsilon = 3$ °C/s, and $\upsilon = 6$ °C/s. The bright, dark blue and purple areas correspond to the distribution of C concentration in cementite, ferrite, and austenite, respectively. The simulation results reveal that at a given phase transformation temperature, an escalation in the cooling rate results in an enhanced C element within the cementite phase. Under a fixed cooling rate, the concentration of the C element diffuses between austenite and pearlite as the phase transformation temperature decreases. This diffusion process continues until the pearlite phase transformation reaches its equilibrium state and concludes.

Fig. 8 illustrates the average distribution curves of C concentration in austenite and ferrite at cooling rates of $\upsilon = 1$ °C/s, $\upsilon = 3$ °C/s, and $\upsilon = 6$ °C/s. Fig. 8(a) represents the average distribution of C concentration in austenite, which increases during the initial stage of pearlite transformation. With the temperature decrease, the C concentration in austenite increase first and then decreases, with the peak values of C concentrations corresponding to different cooling rates of 1 °C/s, 3 °C/s, and 6 °C/s are 0.91 wt.%, 1.20 wt.%, and 2.18 wt.%, respectively. Furthermore, the peak of C concentration shifts towards lower temperatures direction as the cooling rate increase. Fig. 8(b) presents the average distribution of C concentration in ferrite. During the preliminary stages of pearlite phase transformation, a slight decrease in C concentration within the ferrite phase is observed. With the cooling rate increase, the peak C concentration in ferrite is recorded as 0.0171 wt.%, 0.0162 wt.%, and 0.0159 wt.%, corresponding to phase transformation temperatures of 700 °C, 673 °C, and

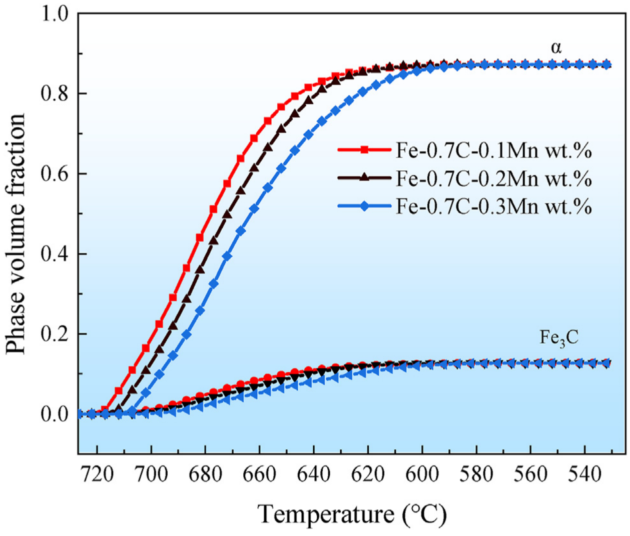

Fig. 10 – The evolution curves depicting the changes of cementite and ferrite phase volume fractions with respect to different Mn content during the austenite-pearlite transformation.

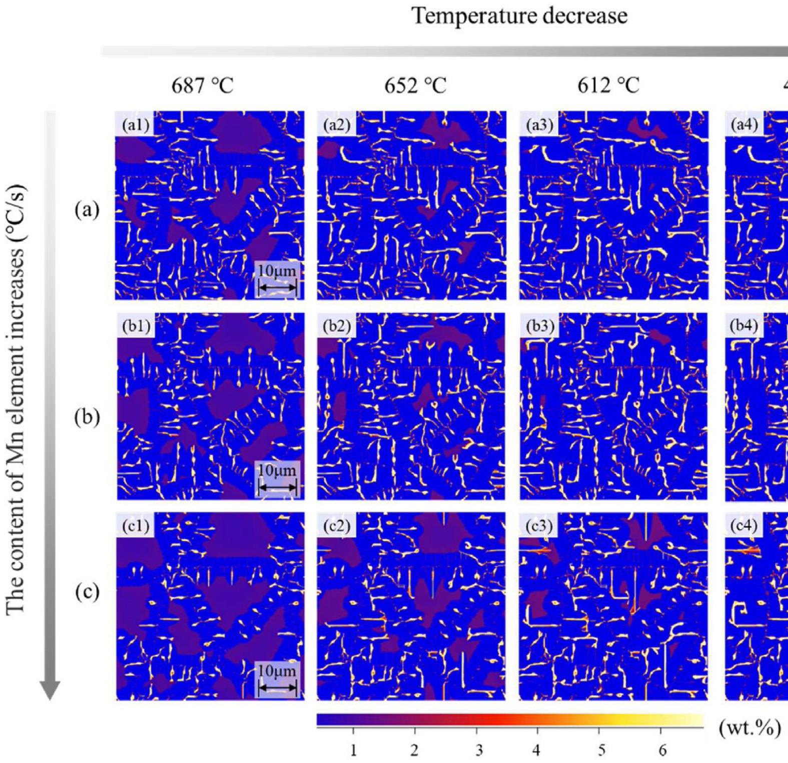

Fig. 11 – The effect of Mn content, (a) Fe-0.7C-0.1Mn wt.%, (b) Fe-0.7C-0.2Mn wt.%, (c) Fe-0.7C-0.3Mn wt.%, on the temporal evolution of C concentration.

643 °C, respectively. In other words, as the cooling rate increases, the peak value of C concentration in ferrite decreases whereas that in austenite increases, and the C concentration in ferrite is about 0 wt.% after the austenite-pearlite transformation.

3.3. *Influence of Mn content on austenite-pearlite transformation*

The microstructural evolution of the austenite-pearlite transformation in polycrystalline materials was examined using a Fe-0.7C-xMn ($x = 0.1, 0.2, 0.3$) wt.% ternary alloy. Fig. 9 illustrates the influence of the Mn element on pearlite phase transformation behavior at a cooling rate $\upsilon = 1$ °C/s and different transformation temperatures. The results indicate that pearlite (an integration of ferrite and cementite) nucleates at the boundaries of austenite. Initially, the phase transformation rate of the austenite-pearlite transformation is rapid. However, as the temperature decreases, the interfacial mobility decreases significantly, resulting in a deceleration of the phase transformation process. The austenite-pearlite transformation in the Fe-0.7C-xMn wt.% ternary alloy yields a divergent pearlite structure. An increase of Mn content tends to lower the austenite-pearlite transformation temperature, extend the phase transformation incubation period, and subsequently delay the transformation process.

Fig. 10 presents the evolution curve of cementite and ferrite phase volume fractions in relation to different Mn content during the austenite-pearlite transformation process. Observations indicate that the phase transformation temperature of pearlite decreases from 712 °C to 702 °C as the Mn content increased from 0.1 wt.% to 0.3 wt.%. At a given pearlite transformation temperature, the phase volume fractions of ferrite and cementite are found to decrease with the increase of the Mn element. Upon reaching a pearlite transformation temperature of 590 °C, the austenite-pearlite phase transformation concludes and the volume fraction of each phase stabilizes.

Fig. 11 illustrates the evolution of C concentration under varied Mn contents at a cooling rate $\upsilon = 1$ °C/s. The brighter regions in the figure represent the distribution of C in cementite, the dark blue regions indicate C concentration in ferrite, and the remaining purple areas denote C concentration distribution in austenite. The results reveal that under a constant Mn content, a C concentration segregation in the cementite phase occurs as the austenite-pearlite transformation progresses. Additionally, the diffusion of C from ferrite to the austenite phase is observed during this process. At a given austenite-pearlite transformation temperature, the austenite-pearlite phase transformation temperature decreases with an increase of Mn content. However, the C concentration in cementite remains relatively stable.

To study the effect of Mn concentration on elemental redistribution during pearlite phase transformation, Fig. 12 shows the distribution of average C concentration within austenite and ferrite during the austenite-pearlite

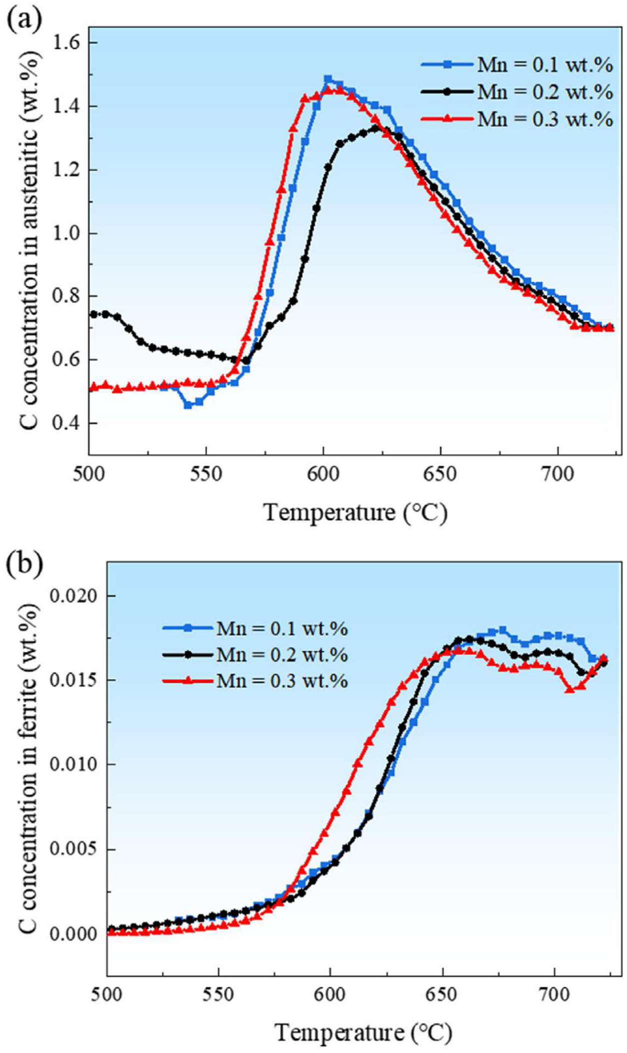

Fig. 12 – The distribution of average C concentration in austenite and ferrite phases at different Mn contents, (a) the average C concentration in the austenite phase, and (b) the average C concentration in the ferrite phase.

transformation. The statistical analysis reveals that the average C concentration in austenite initially increases, followed by a subsequent decrease, with the maximum concentration peak at 1.48 wt.%, 1.33 wt.%, and 1.45 wt.%, respectively (as illustrated in Fig. 12(a)). During the initial stage of austenite-pearlite transformation, fluctuations in the concentration of C in ferrite are observed. As the transformation temperature decreases, the C in ferrite diffuses progressively into the austenite phase (Fig. 12(b)). The research results show that the C concentration in austenite and ferrite in the process of austenite-pearlite transformation shows a trend of increasing first and then decreasing.

4. Conclusions

In the present work, a multi-phase-field simulation was employed to explore the microstructure evolution of austenite-pearlite transformation in polycrystalline pearlite steel. Specifically, the influence of pearlite phase transformation isothermal temperature, cooling rate, and Mn concentration on the microstructure evolution were studied. The transformation of pearlite interlamellar spacing and phase volume fraction with temperature were calculated under various influencing factors. The primary conclusions drawn from this study can be summarized as follows:

(1) With a given austenitizing conditions of isothermal temperature, the decrease in the isothermal temperature of the austenite-pearlite transformation from 710 °C to 690 °C results in a reduction in pearlite interlamellar spacing, which from 0.805 μm to 0.73 μm.
(2) As the phase transformation cooling rate increases from $v = 1$ °C/s to $v = 6$ °C/s, the pearlite interlamellar spacing was refined from 0.83 μm to 0.60 μm, and the peak values of C concentration in the austenite phase was elevated from 0.91 wt.% to 2.18 wt.%.
(3) The addition of Mn from 0.1 wt.% to 0.3 wt.% lowers the pearlite transformation temperature from 712 °C to 702 °C, and extends the incubation period of the pearlite transformation from 15 °C to 25 °C.

Declaration of competing interest

Acknowledgments

This work was supported by the National Key Research and Development Program of China (No. 2021YFB3702401), and the National Natural Science Foundation of China (Nos. 52122408, 51901013, 52071023), H.H. Wu also thanks the financial support from the Fundamental Research Funds for the Central Universities (University of Science and Technology Beijing, No. FRF-TP-2021-04C1 and 06500135). JZ thanks for the support from Zhejiang Lab Open Research Project (No. K2022PE0AB05). The computing work is supported by USTB MatCom of Beijing Advanced Innovation Center for Materials Genome Engineering.

REFERENCES

[1] De Graef M, Kral MV, Hillert M. A modern 3-D view of an "old" pearlite colony. JOM 2006;58:25–8.
[2] Embury D. The formation of pearlite in steels, Phase Transformations in Steels. Woodhead Publ; 2012. p. 276–310.
[3] Seo SW, Bhadeshia HKDH, Suh DW. Pearlite growth rate in Fe-C and Fe-Mn-C steels. Mater Sci Technol 2015;31(4):487–93.
[4] Xu TL, Wang W, Jiang HY, He GZ. Study on micro crack propagation mechanism of ferrite-pearlite gas transmission pipeline steel with lamellar structure. Sci Rep 2022;12(1):18642.

[5] Nakajima K, Tanaka Y, Hosoya Y, Apel M, Steinbach I. Phase-field simulation of cooperative growth of pearlite, Materials Science Forum. Trans Tech Publ 2007;558:1013–20.

[6] Mushongera LT, Amos PGK, Nestler B, Ankit K. Phase-field simulations of pearlitic divergence in Fe-C-Mn steels. Acta Mater 2018;150:78–87.

[7] Cai Q, Pu Y, Tang D, Mi Z, Zhu Y. Effect of continuous cooling conditions on microstructure and mechanical properties of high carbon steel rod. Int J Miner Metall Mater 1999;6(4):277–80.

[8] Ankit K, Choudhury A, Qin C, Schulz S, McDaniel M, Nestler B. Theoretical and numerical study of lamellar eutectoid growth influenced by volume diffusion. Acta Mater 2013;61(11):4245–53.

[9] Steinbach I, Apel M. The influence of lattice strain on pearlite formation in Fe-C. Acta Mater 2007;55(14):4817–22.

[10] Zhang XD, Godfrey A, Hansen N, Huang XX. Hierarchical structures in cold-drawn pearlitic steel wire. Acta Mater 2013;61(13):4898–909.

[11] Ji X, Zhao S, Fu L, Peng J, Gao J, Yu D, et al. High cycle rotating bending fatigue performance and fracture behavior in a pearlite-ferrite dual-phase steel. J Iron Steel Res Int 2022;29:519–28.

[12] Wang L, Tang D, Song Y. Prediction of mechanical behavior of ferrite-pearlite steel. J Iron Steel Res Int 2017;24(3):321–7.

[13] Dong C, Wu H, Wang X. Effect of cooling rate on microstructure, hardness, and residual stress of 0.28 C-0.22 Ti wear-resistant steel. J Iron Steel Res Int 2019;26:866–74.

[14] Wang Y, Chen Y, Yu W. Effect of Cr/Mn segregation on pearlite-martensite banded structure of high carbon bearing steel. Int J Miner Metall Mater 2021;28(4):665–75.

[15] Aranda M, Rementeria R, Poplawsky J, Urones-Garrote E, Capdevila C. The role of C and Mn at the austenite/pearlite reaction front during non-steady-state pearlite growth in a Fe-C-Mn steel. Scripta Mater 2015;104:67–70.

[16] Miyamoto G, Karube Y, Furuhara T. Formation of grain boundary ferrite in eutectoid and hypereutectoid pearlitic steels. Acta Mater 2016;103:370–81.

[17] Chen LQ. Phase-field models for microstructure evolution. Annu Rev Mater Res 2002;32(1):113–40.

[18] Lv SJ, Wang SZ, Wu GL, Gao JH, Yang XS, Wu HH, et al. Application of phase-field modeling in solid-state phase transformation of steels. J Iron Steel Res Int 2022;29(6):867–80.

[19] Wang K, Yan C, Yuan C, Yang X, Zhao L, Wang Q. Progress in research on diffusional phase transformations of Fe-C alloys under high magnetic fields. J Iron Steel Res Int 2022;29(5):707–18.

[20] Lu F, Wen L, Han X, Jiang W, Duan H, Xu J, et al. Phase-field method for growth of iron whiskers in the presence of CO gas convection. J Iron Steel Res Int 2019;26(8):829–37.

[21] Kang Y, Jin Y, Zhao Y, Hou H, Chen L. Phase-field simulation of tip splitting in dendritic growth of Fe-C alloy. J Iron Steel Res Int 2017;24(2):171–6.

[22] Deng H, Wang L, Liu Y, Song X, Meng F, Huang S. Evolution behavior of γ''phase of IN718 superalloy in temperature/stress coupled field. Int J Miner Metall Mater 2021;28:1949–56.

[23] Ma Y, Zheng R, Gao Z, Krupp U, Luo H, Song W, et al. Multiphase-field simulation of austenite reversion in medium-Mn steels. Int J Miner Metall Mater 2021;28(5):847–53.

[24] Lai K, Shi S, Yan Z, Li Y, Jin S, Wang D, et al. Phase-field simulation of re-dissolution of γ' phase in Ni-Al alloy by continuous and second-order aging treatment. Rare Met 2021;40:1155–63.

[25] Su M, Zheng L, Lang Z, Yan J, Zhang H. Microstructural evolution of a PM TiAl alloy during heat treatment in $\alpha+\gamma$ phase field. Rare Met 2012;31:424–9.

[26] Militzer M. Phase field modeling of microstructure evolution in steels. Curr Opin Solid State Mater Sci 2011;15(3):106–15.

[27] Zhang Z, Hu C, Zhou A, Xu Y, Wu Y, Huang H, et al. Computer simulation of super-magnetoelastic behavior near critical region of magnetic materials based on phase-field method. Rare Met 2023:1–12.

[28] Yang C, Xu Q, Liu B. Phase-field–lattice Boltzmann simulation of dendrite growth under natural convection in multicomponent superalloy solidification. Rare Met 2020;39(2):147–55.

[29] Yang WK, Jiang X, Tian XL, Hou H, Zhao YH. Phase-field simulation of nano-α'precipitates under irradiation and dislocations. J Mater Res Technol 2023;22:1307–21.

[30] Chen W, Hou H, Zhang Y, Liu W, Zhao Y. Thermal and solute diffusion in α-Mg dendrite growth of Mg-5wt.% Zn alloy: a phase-field study. J Mater Res Technol 2023;24:8401–13.

[31] Zhao Y. Co-precipitated Ni/Mn shell coated nano Cu-rich core structure: a phase-field study. J Mater Res Technol 2022;21:546–60.

[32] Nakajima K, Apel M, Steinbach I. The role of carbon diffusion in ferrite on the kinetics of cooperative growth of pearlite: a multi-phase field study. Acta Mater 2006;54(14):3665–72.

[33] Chabak Y, Shimizu K, Efremenko V, Golinskyi M, Kusumoto K, Zurnadzhy V, et al. Microstructure and phase elemental distribution in high-boron multi-component cast irons. Int J Miner Metall Mater 2022;29(1):78–87.

[34] Meng Q, Xu J, Li H, Zhao C, Qi J, Wei F, et al. Phase transformations and mechanical properties of a Ti36Nb5Zr alloy subjected to thermomechanical treatments. Rare Met 2022;41(1):209–17.

[35] Xie X, Fang G, Hu Y, Cao X, Zhu T, Pan A. Complementary two-phase anode improving stability and conductivity for lithium storage performance. Rare Met 2023;42(1):85–99.

[36] Yamanaka A, Yamamoto T, Takaki T, Tomita Y. Multi-phase-field study for pearlite transformation with grain boundary diffusion. Florida, USA: Proc 4th Int Conf Multiscale Mater Model (MMM2008); 2008.

[37] Steinbach I, Pezzolla F, Nestler B, Seeßelberg M, Prieler R, Schmitz GJ, et al. A phase field concept for multiphase systems. Phys Nonlinear Phenom 1996;94(3):135–47.

[38] Steinbach I, Zhang LJ, Plapp M. Phase-field model with finite interface dissipation. Acta Mater 2012;60(6–7):2689–701.

[39] Steinbach I, Apel M. Multi phase field model for solid state transformation with elastic strain. Phys Nonlinear Phenom 2006;217(2):153–60.

[40] Ta N, Zhang LJ, Du Y. Design of the precipitation process for Ni-Al alloys with optimal mechanical properties: a phase-field study. Metall Mater Trans A 2014;45(4):1787–802.

[41] Bouzouni M, Gavalas E, Papaefthymiou S. Modeling the microstructure evolution during quenching & partitioning of a conventional CrMo alloy steel. Comput Mater Sci 2022;206:111265.

[42] Ta N, Zhang LJ, Tang Y, Chen WM, Du Y. Effect of temperature gradient on microstructure evolution in Ni-Al-Cr bond coat/substrate systems: a phase-field study. Surf Coat Technol 2015;261:364–74.

[43] Steinbach I. Phase-field models in materials science. Model Simulat Mater Sci Eng 2009;17(7):073001.

[44] Eiken J, Böttger B, Steinbach I. Multiphase-field approach for multicomponent alloys with extrapolation scheme for numerical application. Phys Rev E 2006;73(6):066122.

[45] Lv SJ, Wu HH, Wang KY, Wang SZ, Wu GL, Gao JH, et al. The microstructure evolution and influence factors of acicular ferrite in low alloy steels. Comput Mater Sci 2023;218:111989.

[46] Lv SJ, Wu HH, Wang KY, Zhu JM, Wang SZ, Wu GL, et al. The austenite to polygonal ferrite transformation in low-alloy steel: multi-phase-field simulation. J Mater Res Technol 2023;24:9630–43.

[47] Chen L, Zhao Y. From classical thermodynamics to phase-field method. Prog Mater Sci 2022;124:100868.

[48] Zhang LJ, Steinbach I, Du Y. Phase-field simulation of diffusion couples in the Ni-Al system. Int J Mater Res 2011;102(4): 371–80.

[49] Nakada N, Kato M. Internal stress and elastic strain energy in pearlite and their accommodation by misfit dislocations. ISIJ Int 2015;56(10):1866–73.

[50] Apel M, Benke S, Steinbach I. Virtual dilatometer curves and effective Young's modulus of a 3D multiphase structure calculated by the phase-field method. Comput Mater Sci 2009;45(3):589–92.

[51] Ferreira VM, Mecozzi MG, Petrov RH, Sietsma J. Details of pearlite to austenite transformation in steel: experiments and phase-field modeling. Comput Mater Sci 2023;228:112368.

[52] Mecozzi MG, Militzer M, Sietsma J, Van der Zwaag S. The role of nucleation behavior in phase-field simulations of the austenite to ferrite transformation. Metall Mater Trans A 2008;39:1237–47.

[53] Laschet G, Apel M. Thermo-elastic homogenization of 3-D steel microstructure simulated by the phase-field method. Steel Res Int 2010;81(8):637–43.

[54] Wang KY, Lv SJ, Wu HH, Wu GL, Wang SZ, Gao JH, et al. Recent research progress on the phase field model of microstructure evolution during metal solidification. Int J Miner Metall Mater 2023. https://doi.org/10.1007/s12613-023-2710-x.